Electronic Supplementary Material (ESI) for Journal of Materials Chemistry A.

Supporting Information

Electrochemical reduction of carbon dioxide with nearly 100% carbon monoxide faradaic efficiency from vacancy-stabilized single-atom active sites

Chenbao Lu [a], Kaiyue Jiang [a], Diana Tranca [a], Ning Wang [b], Hui Zhu [c], Fermín Rodríguez-Hernández [d], Zhenying Chen [a], Chongqing Yang [a], Fan Zhang * [a], Yuezeng Su [e], Changchun Ke * [f], Jichao Zhang * [g], Yu Han [c], Xiaodong Zhuang *[a]

[a] The meso-Entropy Matter Lab, School of Chemistry and Chemical Engineering, Frontiers Science Center for Transformative Molecules, State Key Laboratory of Metal Matrix Composites, Shanghai Key Laboratory of Electrical Insulation and Thermal Aging, Shanghai Jiao Tong University, 800 Dongchuan Road, Shanghai 200240, China.

E-mail: fan-zhang@sjtu.edu.cn, zhuang@sjtu.edu.cn

[b] Faculty of Environment and Life, Beijing University of Technology, Beijing, 100124, PR China

[c] Advanced Membranes and Porous Materials Center, Division of Physical Sciences and Engineering, King Abdullah University of Science and Technology (KAUST), Thuwal 23955-6900, Kingdom of Saudi Arabia

[d] Departamento de Química, Módulo 13, Universidad Autónoma de Madrid, 28049 Madrid, Spain

[e] School of Electronic Information and Electrical Engineering, Shanghai Jiao Tong University, Shanghai 200240, China.

[f] School of Mechanical Engineering, Shanghai Jiao Tong University, Shanghai 200240, China. E-mail: kechangchun@sjtu.edu.cn

[g] Shanghai Synchrotron Radiation Facility, Zhangjiang Laboratory, Shanghai Advanced Research Institute, Chinese Academy of Sciences, No. 239, Zhangheng Road, Shanghai 201204, China. E-mail: zhangjichao@zjlab.org.cn

Outline

1. Experimental section.

2. Characterization of as-prepared SACs.

3. Tables

1. Experimental section.

1.1. Chemicals:

Ethylenediamine (EDA) and HCl (37 wt.%) were bought from Sinopharm Chemical Reagent. Mg power was purchased from Aladdin Reagent. $NaNO_2$, Nafion solution (5 wt.%), $KHCO_3$, acetylactonate nickel, acetylactonate cobalt, and acetylactonate iron were bought from Sigma-Aldrich.

1.2. Preparation of SACs via self-propagating combustion strategy.

For the synthesis of NiN-C and NiNV-C, acetylactonate nickel (1 g) was dissolved into EDA solution (50 g) followed by ultrasoniccation for 30 min, acetylactonate nickel can be chelated by EDA to form homogeneous pink solution. Then, directly through CO_2 gas into EDA solution, CO_2 can be captured by EDA and formed into carbamate (equation 1), until there were continuous bubbles, indicating the CO_2 saturated. Excessive Mg powders (25 g) were then mixed with the CO_2-saturated EDA solution and heated at 90 ℃ for 10 min, a gel-like organic-metal complex was obtained because of the spontaneous redox reaction between ammonium cationic group and Mg (equation 2). Ignited the obtained mixture, the mixture burned violently and kept approximately 30 seconds, the highest combustion temperature in this work up to ~1000 ℃. The NiN-C was obtained after etching in 1 M HCl for 12 h to remove Mg complex and impurities, the yield of carbon material is calculated as ~25 %. Afterwards, NiN-C was subjected to a second heat treatment under 1000 ℃ at Ar atmosphere for 1 h to obtain NiNV-C.

To prove the universal of such slef-propagating combustion approach, CoNV-C and FeNV-C were also prepared through the same procedure by using acetylactonate cobalt and acetylactonate iron as precursors, respectively. NPC was prepared without adding metal sources.

$$CO_2 + 2NH_2C_2H_4NH_2 \longrightarrow NH_2C_2H_4NHCOO^- + NH_2C_2H_4NH^{3+} \quad (1)$$

$$2NH_2C_2H_4NHCOO^- + 2NH_2C_2H_4NH^{3+} + Mg \longrightarrow (NH_2C_2H_4NHCOO)_2Mg + 2NH_2C_2H_4NH_2 + H2 \quad (2)$$

$$(NH_2C_2H_4NHCOO)_2Mg + 2NH_2C_2H_4NH_2 + \phi Mg + (\phi/2 + 3)O_2 \longrightarrow 10C + (\phi + 1)MgO + 2N_2 + 13H_2O \quad (3)$$

Electrochemical measurements: Electrochemical reduction of CO_2 was firstly performed in H-type three-electrode cell separated by Nafion 117 membrane, Pt mesh as counter electrode, Ag/AgCl as reference electrode, catalysts loaded on carbon paper (1×1 cm^2) as working electrode. The details of preparing working electrode are as follows: 10 mg of catalysts were blended with 1 mL of Nafion solution (0.5 wt. %) and sonicated for 2 h for producing catalyst ink. Then 100 μL of catalyst ink was pipetted onto the carbon paper surface (1 cm^{-2}), giving a catalyst loading of 1 mg cm^{-2}. The electrodes were dried at room temperature before test. All potentials reported in this work were versus to reversible hydrogen electrode (RHE):

$$E_{RHE}\,(V) = E_{Ag/AgCl}\,(V) + 0.197\ V + 0.0591V * pH$$

The electrolyte was CO_2-saturated 0.5 M $KHCO_3$, and CO_2 was continuously supplied to the cell (20 sccm) through a gas bubbling tube during the constant potential electrolysis. The LSV curves were obtained with a scan rate of 5 mV s^{-1}, all potentials in this study were without iR compensated. The electrochemical impedance spectroscopy was measured at instantaneous open circuit potential in the frequency range between 200 kHz and 100 mHz with a perturbation amplitude of 10 mV. The electrochemical double-layer capacitances (C_{dl}) of catalysts were calculated from CV curves. The CV curves were performed at scan rates varying from 5 to 60 mV s^{-1} in the region from 0.30 to 0.50 V. The capacitive currents of ΔJ ($J_{anodic} - J_{cathodic}$) are plotted as a function of the CV against the scan rate. The slope of the fitting line is equal to twice the C_{dl}, which is linearly proportional to the electrochemically effective surface area of the electrode.

The TOF for NiN-C and NiNV-C were calculated as:

$$TOF=(FE*J *A)/(n*F*s*m)$$

Where FE is the Faradaic efficiency of CO production, J is the total current density, A is the electrode geometric area (1 cm^2), ω is the Ni content in the catalysts (analyzed by ICP-AES), n is the number of electros transfer for CO formation (2), F is the faraday constant, m is the mass of catalyst coated on working electrode, and s is the density of active sites.

Flow cell measurements were performed in a home-made flow cell reactor (Fig. 4a). NiNV-C loaded on GDE (1 mg cm^{-2}, 1 × 1 cm^2) as the cathode, anion exchange membrane (1 × 1 cm^2) as the separator, 20 wt% Ir/C loaded on GDE (1 mg cm^{-2}, 1 × 1 cm^2) as the anode, and 1 M KOH as the electrolyte. Peristaltic pumps were used to force the electrolyte circulation to promote the mass transfer and buffer the electrolyte pH change. During the measurements, CO_2 gas can be directly supplied to the catalysts surface at a rate of 20 sccm.

CO-TPD measurement: TPD experiments were performed on Auto Chem II 2920. All samples were thermally pre-treated to remove any possible surface contamination. The CO molecules are dragged by the carrier gas (He) to thermal conductivity detector that measures the signal difference of the desorbed gas versus a reference flow. TPD experiments were carried out up to 700 ℃ with a linear temperature ramp of 10 ℃ min^{-1}.

First-principles calculation:

The calculations of geometry optimization and electronic structure were carried out by density functional theory as implemented in the Vienna ab initio simulation package (VASP) with consideration of spin-polarization, using projector augmented wave (PAW) pseudopotential for the core electrons, a 480 eV cutoff energy for the valence electrons, and the generalized gradient approximation (GGA) in the form of Perdew–Burke–Ernzerhof (PBE) for the exchange-correlation potentials.

The optimized configurations are shown in Fig. 4a. A vacuum space of ~11 Å along the *Z* direction was used to separate the interaction between the neighbouring slabs. The $6 \times 6 \times 1$ gamma-centered *k*-mesh was chosen to sample the surface Brillouin-zone. For the calculation of density of states (DOS), the *k*-mesh was increased to $12 \times 12 \times 1$. The adsorption configurations are fully relaxed until the force on each atom is smaller than 0.01 eV Å^{-1}.

The adsorption energy of reaction intermediates is defined as:

$$E_{ads}=E_{Sub/M} - E_{Sub} - E_M$$

Where $E_{Sub/M}$, E_{Sub} and E_M denote the total energies of an adsorbed system, a clean substrate, and an adsorb at free state, respectively, each of which can be obtained directly from DFT calculations. The adsorption energies are converted into Gibbs free energies through

$$\Delta G=E_{ads} + \Delta ZPE - T\Delta S + \Delta Gu$$

Where ΔZPE, $T\Delta S$, and ΔG_u represent the change of zero-point energy, change of entropy ($T = 298.15$ K), and the contribution of the electrode potential to ΔG, respectively. The zero-point energy is calculated within the harmonic approximation using the finite difference method with displacements of ±0.015 Å.

Characterization

SEM measurements were performed on a FEI Sirion-200 field emission scanning electron microscope. TEM images were acquired using a Tecnai G2 F20 S-TWIN transmission electron microscope (FEI) operated at 200 kV. Aberration-corrected High-angle annular dark-field scanning transmission electron microscopy (HAADF-STEM) images were performed with a Titan Cubed Themis G2 300 (FEI). XRD patterns were performed on a RigakuD/Max 2500 X–ray diffractometer with Cu Karadiation (k=1.54 Å) at age neater voltage of 40 kV and a generator current of 40 mA. X-ray photoemission spectroscopy (XPS) measurements were performed on a PHI–5000C ESCA system, the C 1s value was set at 284.8 eV for charge corrections. The Raman spectra of samples were obtained on Lab-RAM HR800 with excitation by an argon ion laser (532 nm). The physic sorption isotherms were measured via an Auto-sorb-iQA3200-4 sorption analyzer (Quantatech Co., USA) based on N_2 adsorption/desorption at 77 K. XANES and EXAFS measurements were tested on the BL14W1 beamline at Shanghai Synchrotron Radiation Facility (SSRF).

2. Characterizations of as-prepared materials

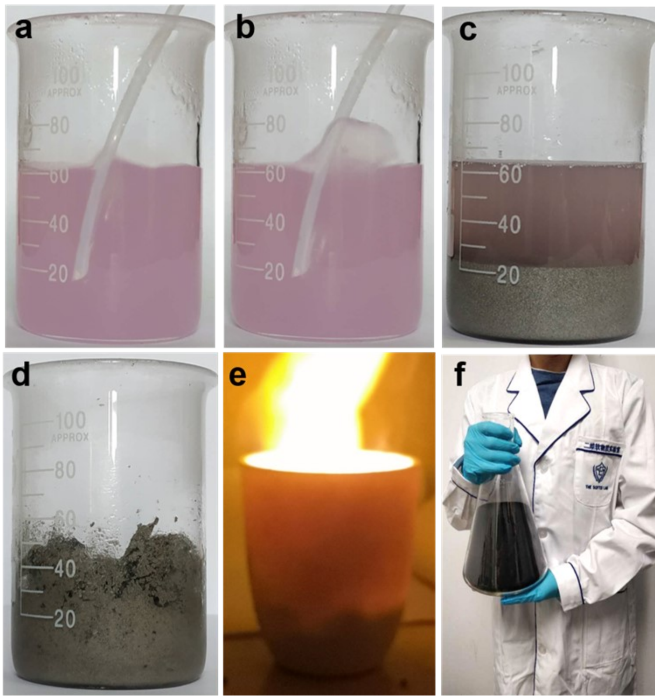

Fig. S1. Photographs for preparation procedure of SACs. a) EDA solution was employed to chelate Ni ions and capture CO_2. **b)** CO_2-saturated EDA solution. **c)** Mix CO_2-saturated EDA solution with Mg powder. **d)** Heat CO_2-saturated EDA solution and Mg powder mixture under 90 ℃ for 10 mins, a gel-like organic-metal complex can be obtained. **e)** Self-propagating combustion in air atmosphere. **f)** Photograph for NiNV-C. It easily amplifies, which is a facile and efficient approach for preparation of SACs in large quantities (kg level).

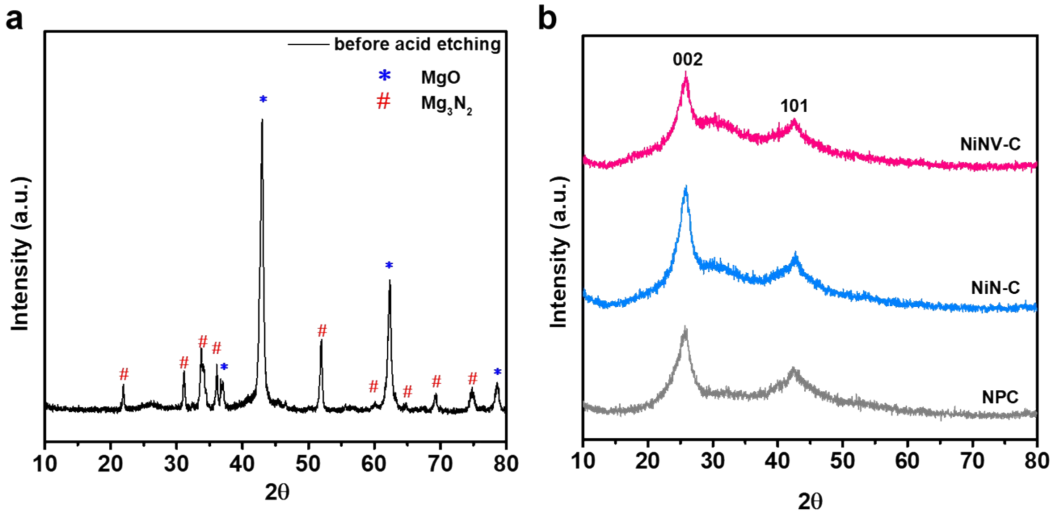

Fig. S2. XRD patterns of as-prepared materials. a) XRD pattern measured after magnesium consuming (without acid etching), only MgO (JCPDS No. 43-1022) and Mg_3N_2 (JCPDS No. 01-1289) peaks can be observed, which result from magnesium burning in the air. No Ni or Ni-based complex diffraction peaks appeared in XRD pattern, indicating that the instant combustion of Mg and the strong interaction between EDA and Ni favor to disperse and stabilize Ni atoms into carbon skeleton. **b)** XRD patterns for NPC, NiN-C and NiNV-C, two peaks located at ~26° and ~43° were observed, which can be ascribed to (002) and (101) planes of graphitic carbon.

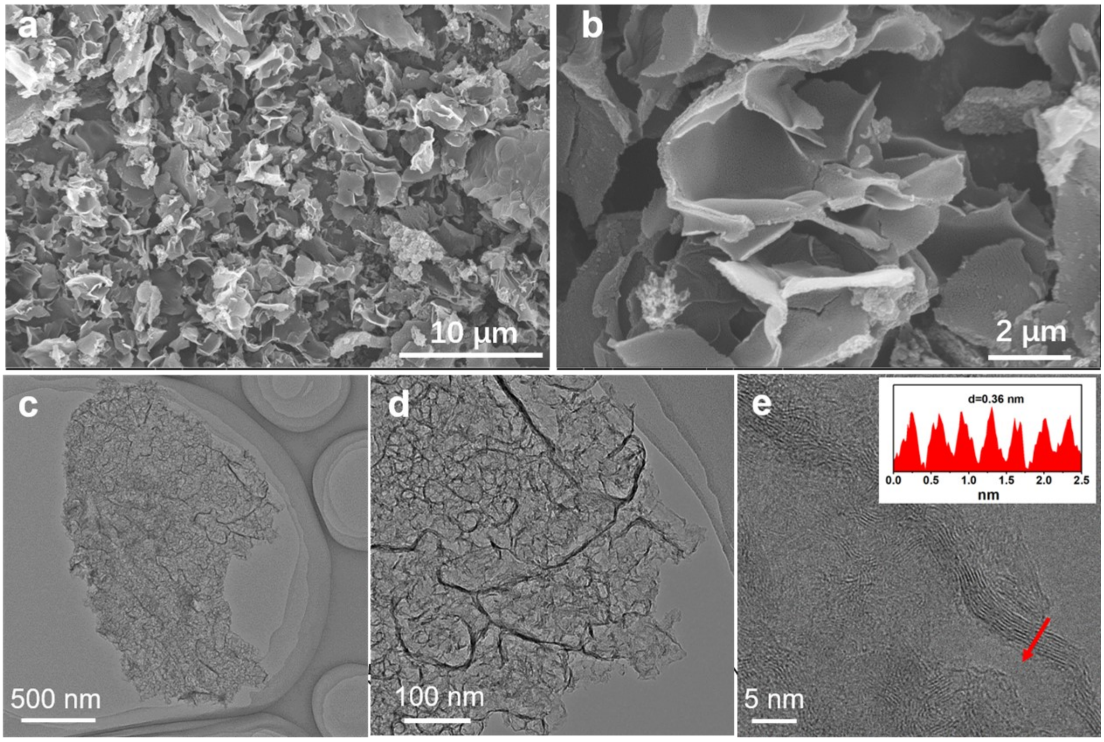

Fig. S3. SEM and TEM images of NiNV-C. a) and **b)** SEM images of NiNV-C. **c)**, **d)** and **e)** TEM images of NiNV-C. Both SEM and TEM images show the 2D morphologies for NiNV-C, no metal nanoparticles or clusters were observed in the TEM images.

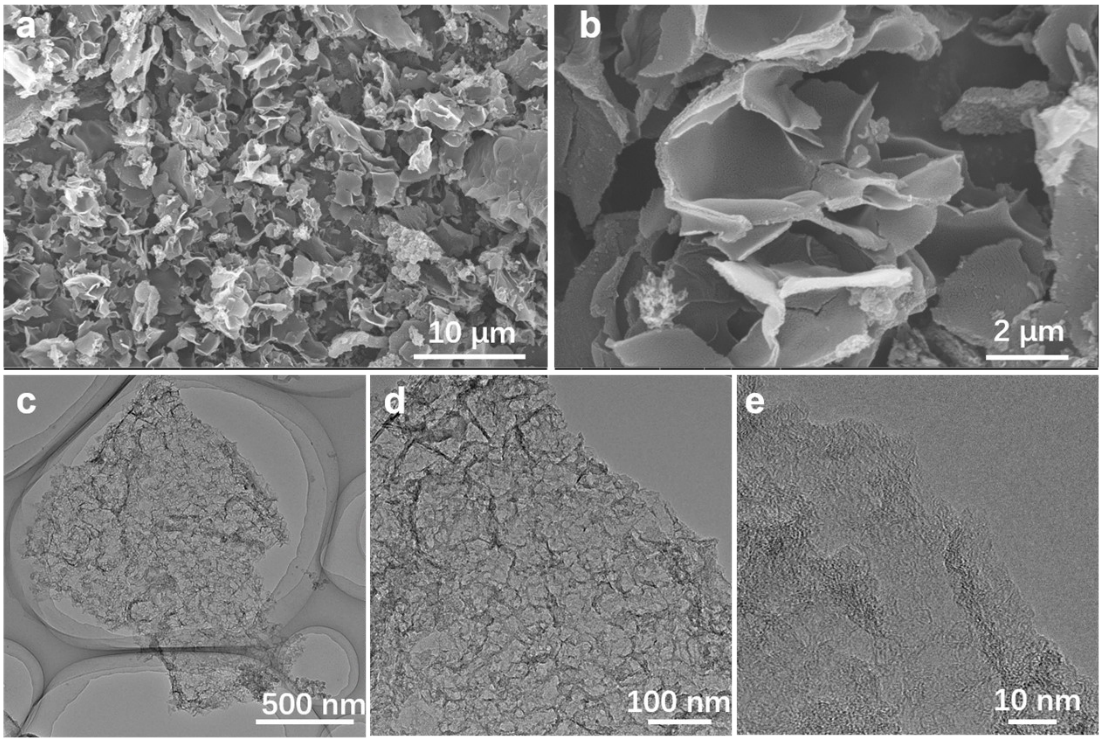

Fig. S4. SEM and TEM images of NiN-C. a) and **b)** SEM images of NiN-C. **c)**, **d)** and **e)** TEM images of NiN-C. Both SEM and TEM images show the 2D morphology for NiN-C, no metal nanoparticles or clusters were observed in the TEM images.

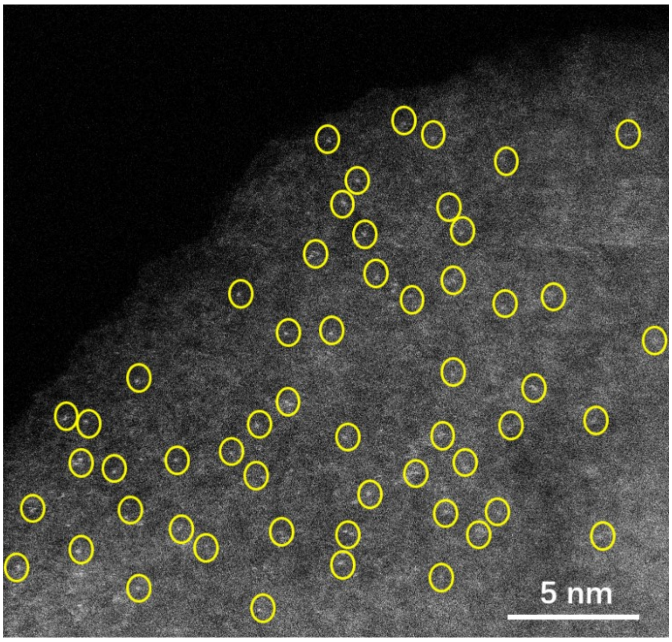

Fig. S5. HAADF-STEM image of NiN-C. Clear light spots (~0.2 nm) were uniformly dispersed on the material, indicating the atomic dispersion of Ni in NiN-C.

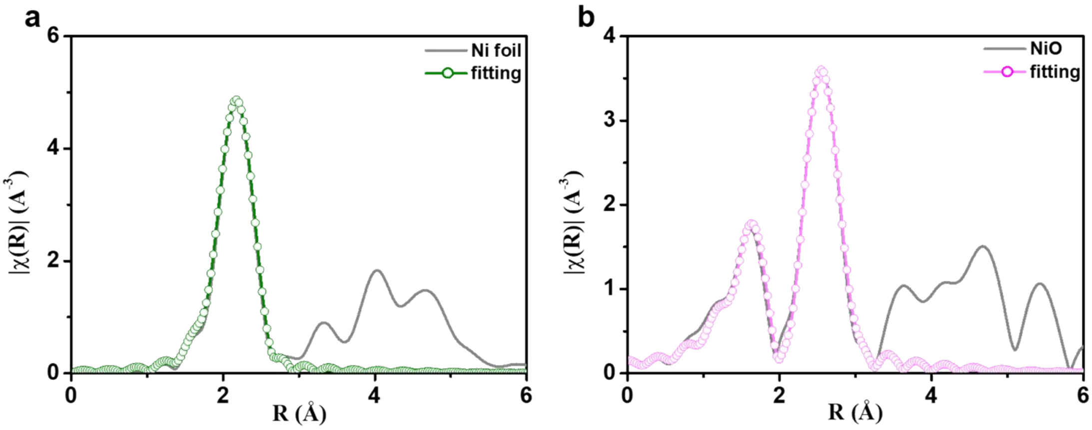

Fig. S6. Fitting of Fourier transformation of EXAFS spectra. a) Fitting of Fourier transformation of EXAFS spectrum for Ni-foil (gray: experimental result, green: fitting result), the main peak appeared at ~2.15Å can be assigned to Ni-Ni interaction. **b)** Fitting of Fourier transformation of EXAFS spectrum for NiO, (gray: experimental result, pink: fitting result). The details of fitting results were summary in Supplementary Table 1.

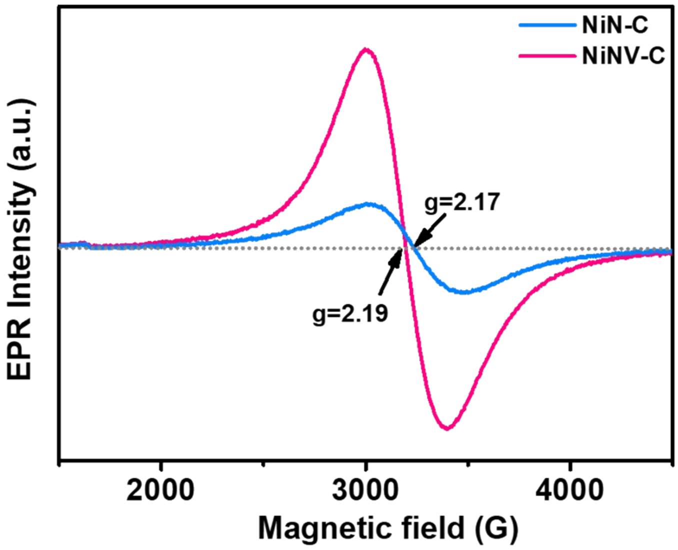

Fig. S7. EPR spectra of NiN-C and NiNV-C. The *g* valve of 2.17 (NiN-C) and 2.19 (NiNV-C) in EPR spectra can be assigned to unpaired electrons in Ni 3*d* orbitals. NiNV-C displayed relative higher intensity than that of NiN-C, revealing more unpaired 3*d* electrons produced in NiNV-C.

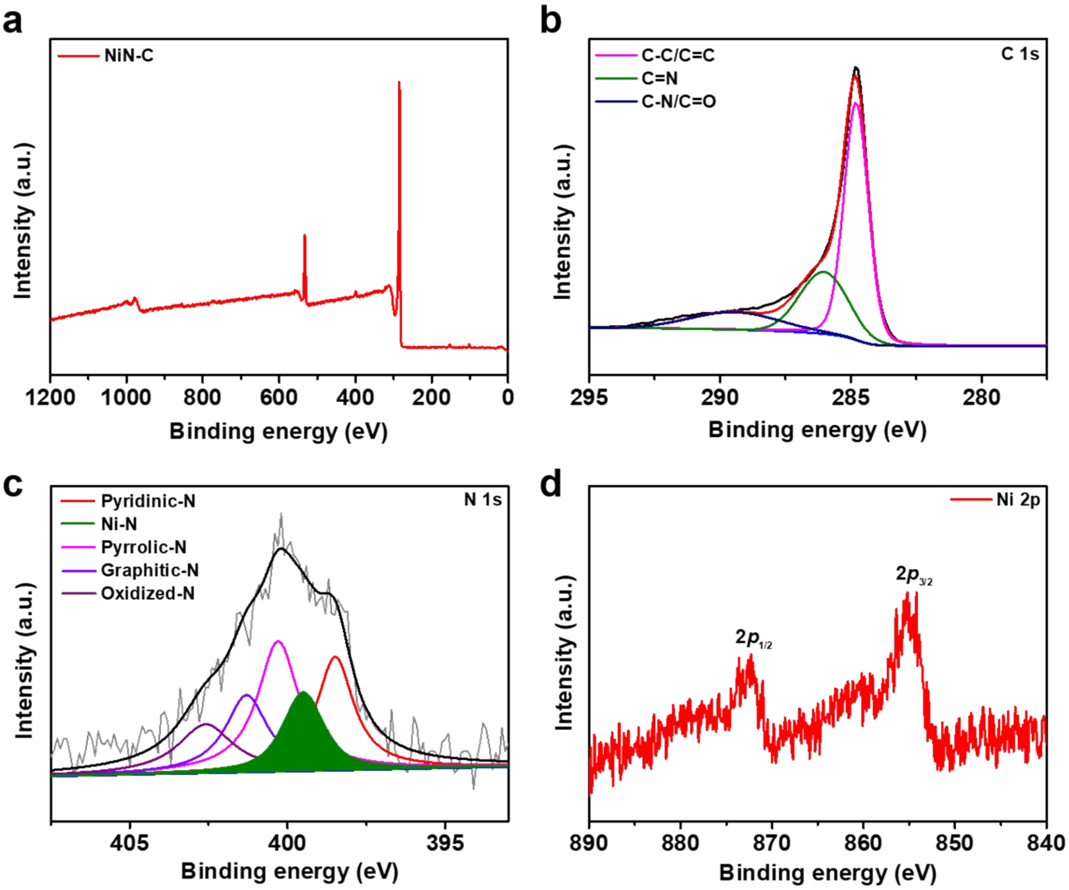

Fig. S8. XPS spectra of NiN-C. a) XPS spectrum of NiN-C. **b)** High-resolution C 1s spectrum of NiN-C. The peak can be divided into three peaks at 284.8, 285.6, and 288.8 eV, corresponding to the C−C/C=C, C=N, and C=O/C-N species, respectively. **c)** High-resolution N 1s spectrum of NiN-C. The peaks can be fitted to five characteristic peaks, including pyridinic-N (~398.6 eV), Ni-N (~399.5 eV), pyrrolic-N (~400.5 eV), graphitic-N (~401.4 eV) and oxidized-N (~402.6 eV), respectively. **d)** High-resolution Ni 2p spectrum of NiN-C. The Ni $2p_{3/2}$ located at ~855.0 eV is higher than that of Ni^0 (853.5 eV) but lower than that of Ni^{2+} (856.0 eV), indicating the valence state of Ni is +1.

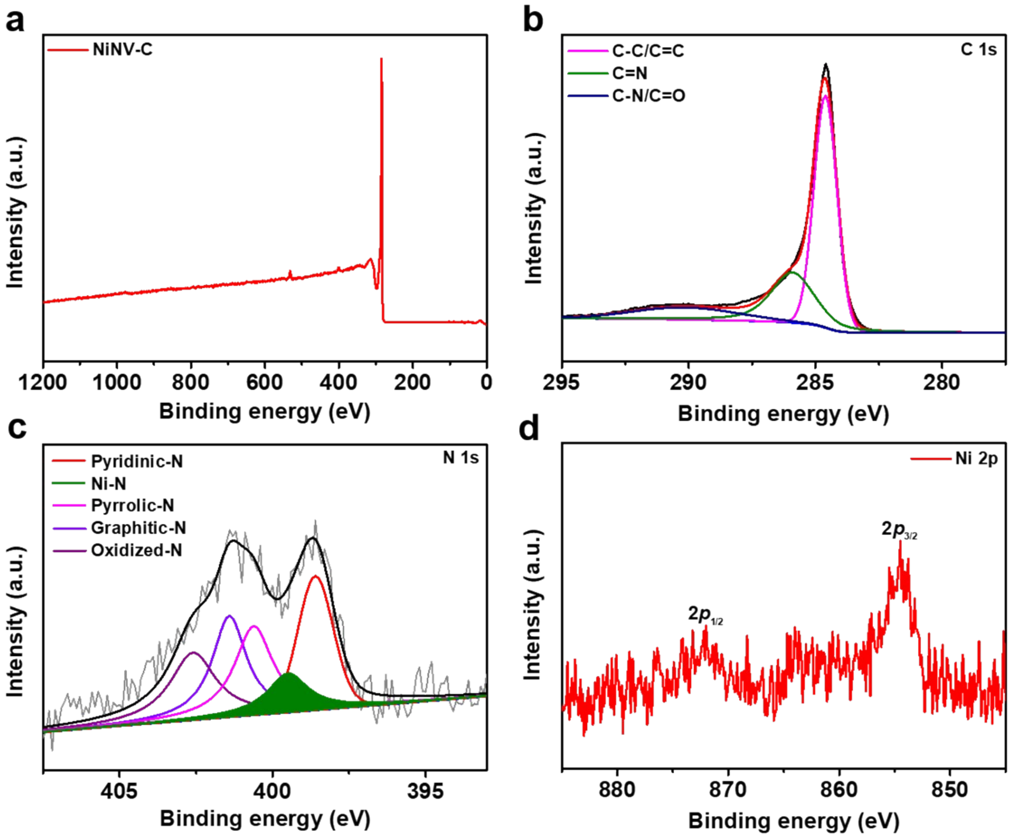

Fig. S9. XPS spectra of NiNV-C. a) XPS spectrum of NiNV-C. **b)** High-resolution C 1s spectrum. The peak can be divided into three peaks at 284.8, 285.6, and 288.8 eV, corresponding to the C−C/C=C, C=N, and C=O/C-N species, respectively. **c)** High-resolution N 1s spectrum. The peaks can be fitted to five characteristic peaks, including pyridinic-N (~398.6 eV), Ni-N (~399.5 eV), pyrrolic-N (~400.5 eV), graphitic-N (~401.4 eV) and oxidized-N (~402.6 eV), respectively. Notably, the contents of Ni-N species in NiNV-C are lower than that of NiN-C, which can be attributed to the second heat treatment under high temperature. **D)** High-resolution Ni 2p spectrum of NiNV-C.

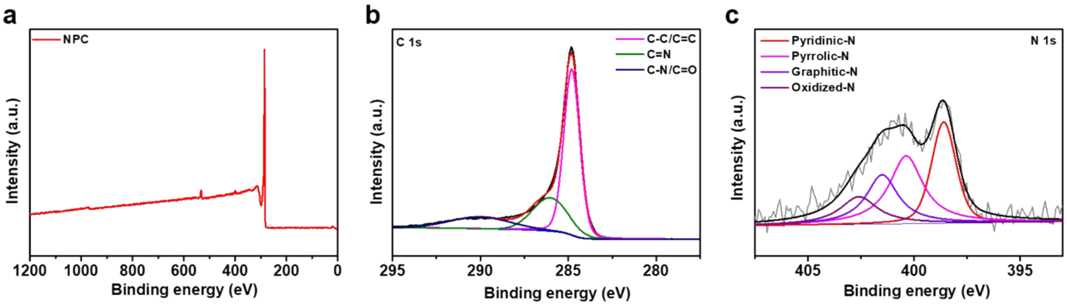

Fig. S10. XPS spectra of NPC. a) XPS spectrum of NPC. **b)** High-resolution C 1s spectrum. **c** High-resolution N 1s spectrum. The peaks can be fitted into pyridinic-N (~398.6 eV), pyrrolic-N (~400.5 eV), graphitic-N (~401.4 eV), and oxidized-N (~402.6 eV) species, respectively.

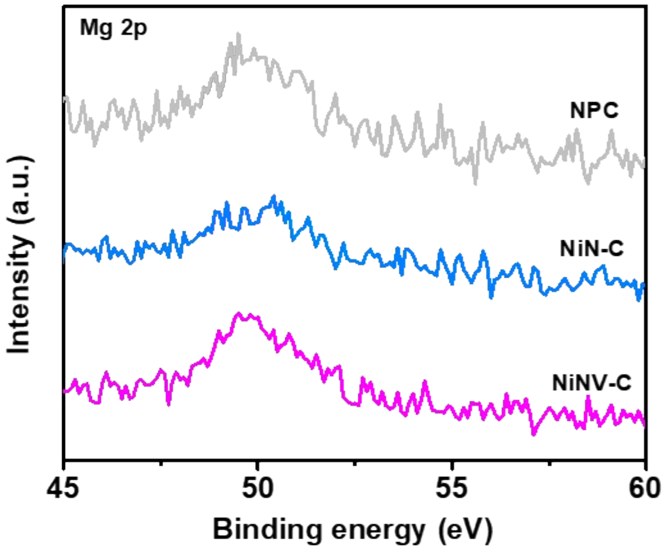

Fig. S11. High-resolution Mg 2p spectra of NPC, NiN-C, and NiNV-C. The Mg contents for NPC, NiN-C, and NiNV-C are 0.70, 0.66, and 0.63 wt%, respectively (Table S4).

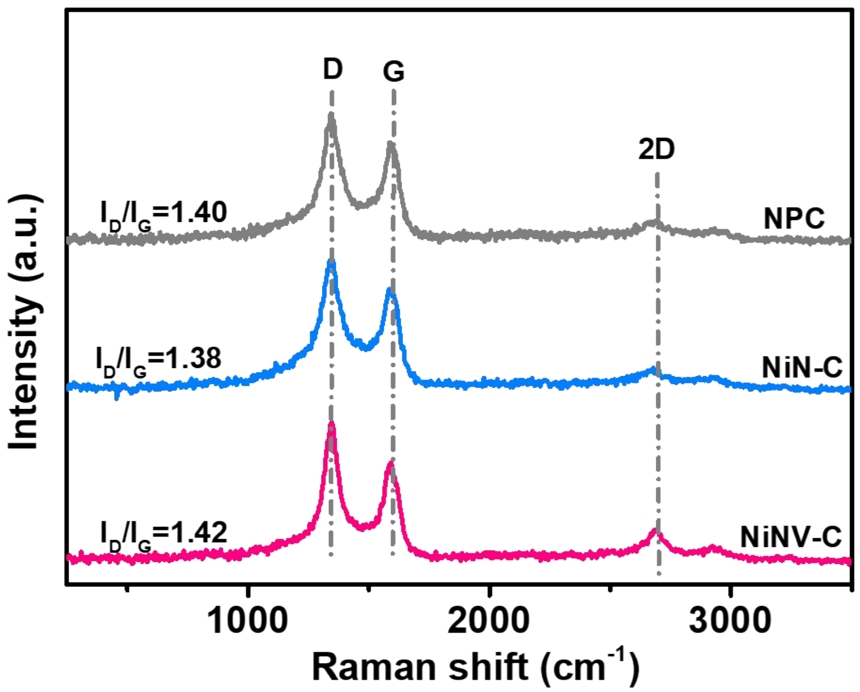

Fig. S12. Raman spectra of NiN-C, NiNV-C, and NPC. the I_D/I_G values for NiN-C, NiNV-C, and NPC were measured as 1.38, 1.42, and 1.40, respectively, indicating that plenty defects produced in obtained materials. A weak 2D band was also observed at ~2682 cm^{-1}, revealing the formation of multilayer graphene due to the template effect of MgO.

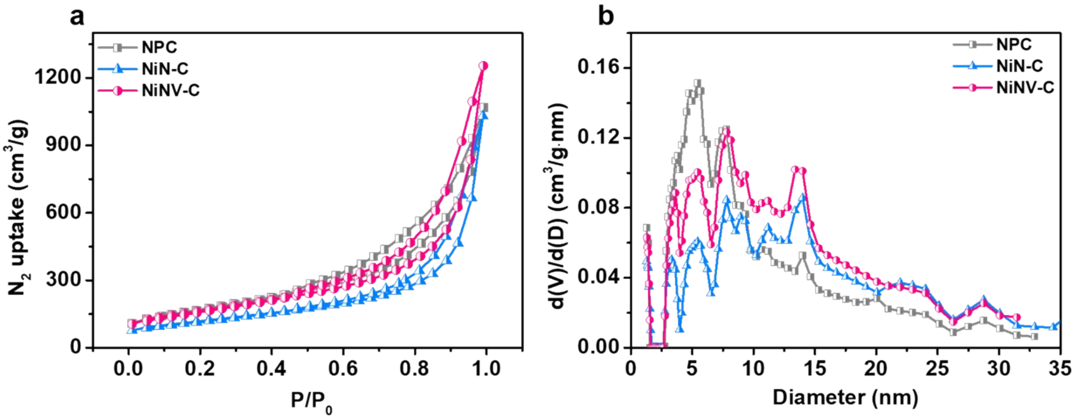

Fig. S13. a) Nitrogen adsorption/desorption isotherms of NiN-C, NiNV-C, and NPC. The specific surface area of NiN-C, NiNV-C, and NPC were calculated as 566, 586 and 617 m^2 g^{-1}, respectively. **b)** Pore size distribution of NiN-C, NiNV-C, and NPC calculated from NLDFT method, the pores in materials were mostly distributed between 2-20 nm, revealing the mesoporous structure.

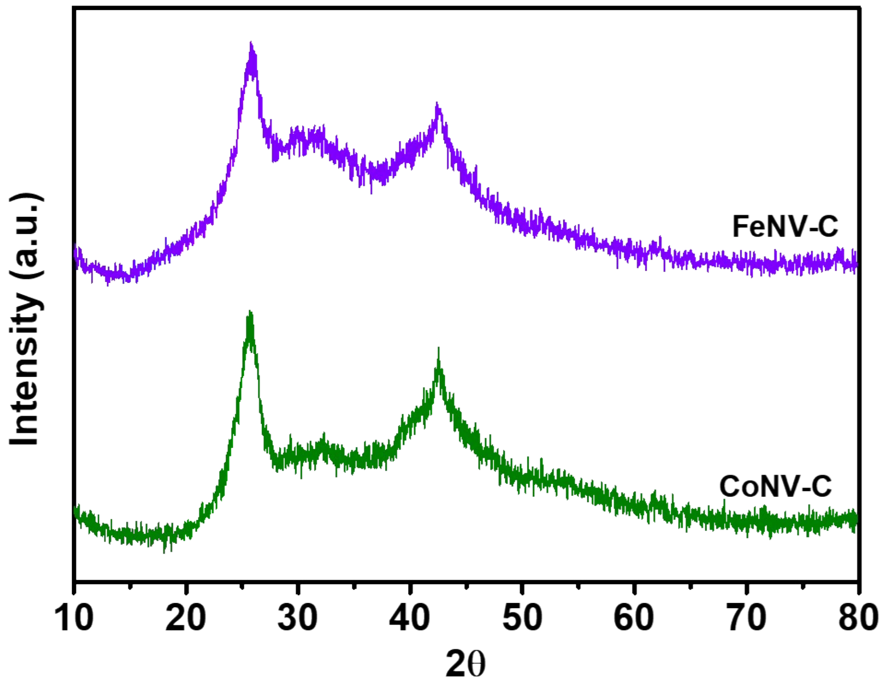

Fig. S14. XRD patterns of FeNV-C and CoNV-C. Two peaks located at ~26° and ~43°can be ascribed to (002) and (101) planes of graphitic carbon, no metal characteristic peaks can be observed.

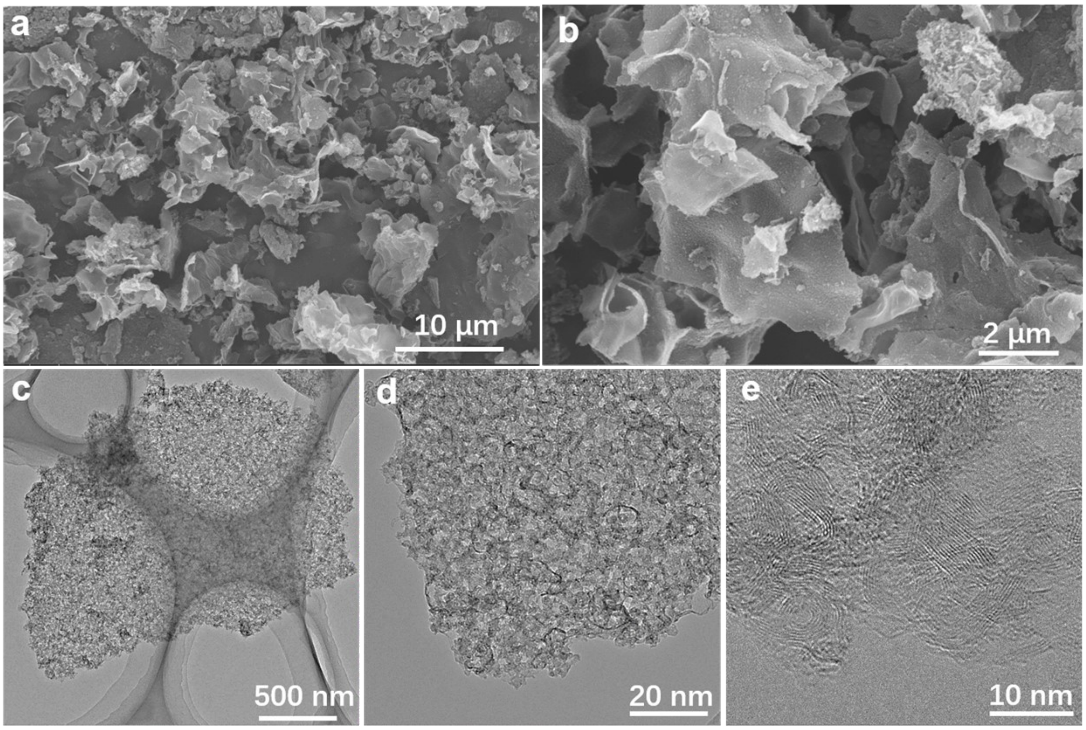

Fig. S15. SEM and TEM images of CoNV-C. a) and **b)** SEM images of CoNV-C. **c)**, **d)** and **e)** TEM images of CoNV-C. Both SEM and TEM images reveal the 2D morphology for CoNV-C.

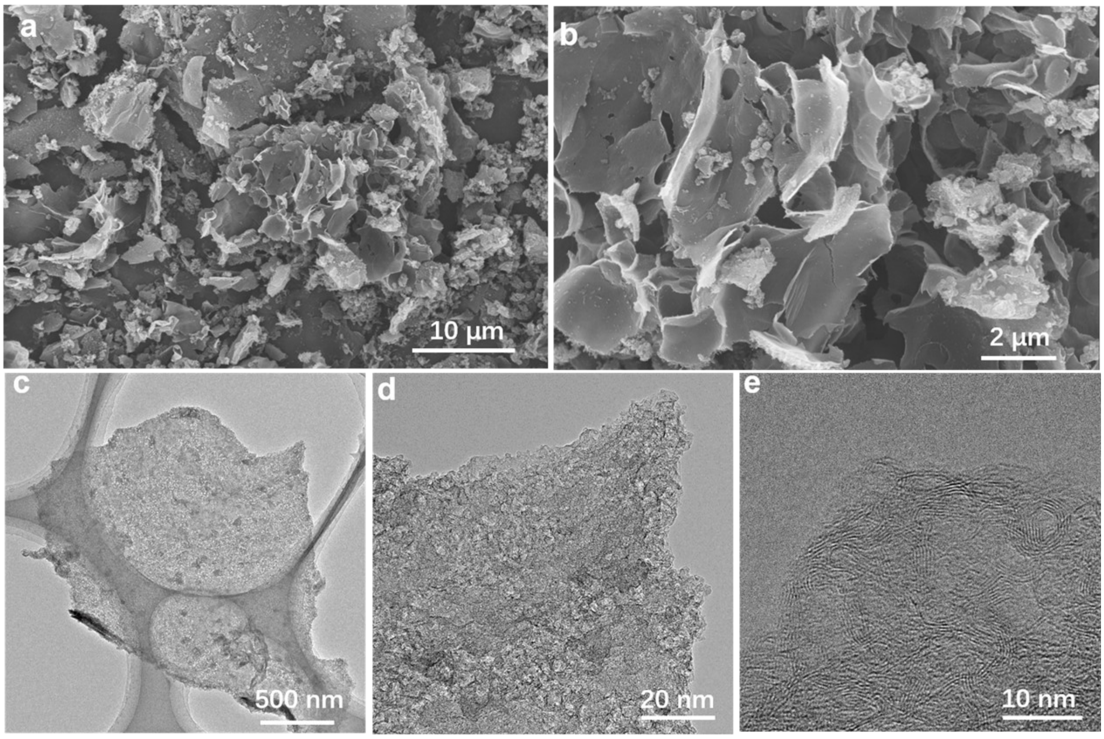

Fig. S16. SEM and TEM images of FeNV-C. a) and **b)** SEM images of FeNV-C. **c)**, **d)** and **e)** TEM images of FeNV-C. SEM and TEM images reveal the 2D morphology for FeNV-C.

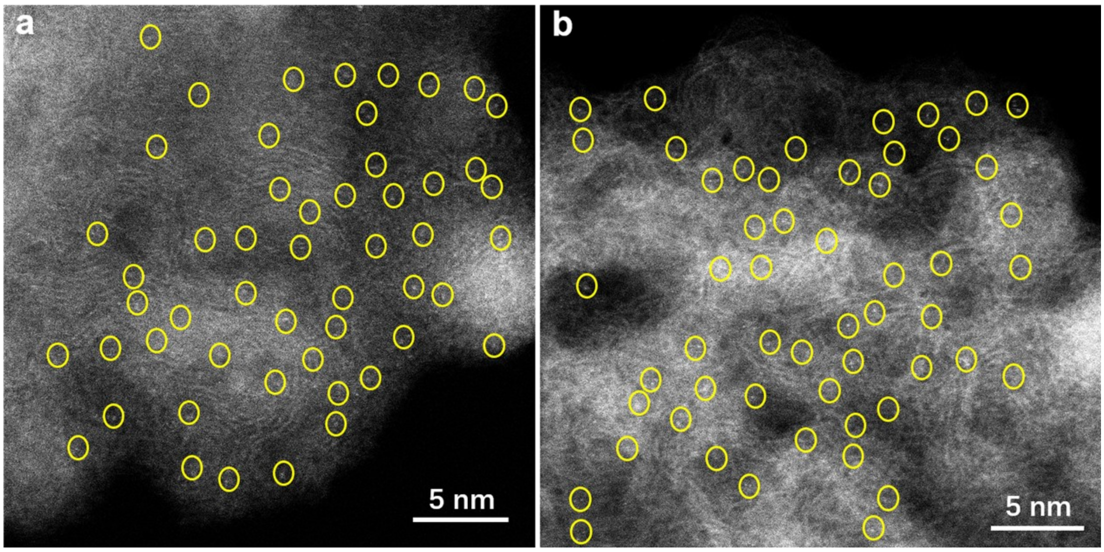

Fig. S17. a) HAADF-STEM image of CoNV-C. **b)** HAADF-STEM image of FeNV-C. Clear light spots were uniformly dispersed on the materials, demonstrating the atomic dispersion of Co and Fe atoms.

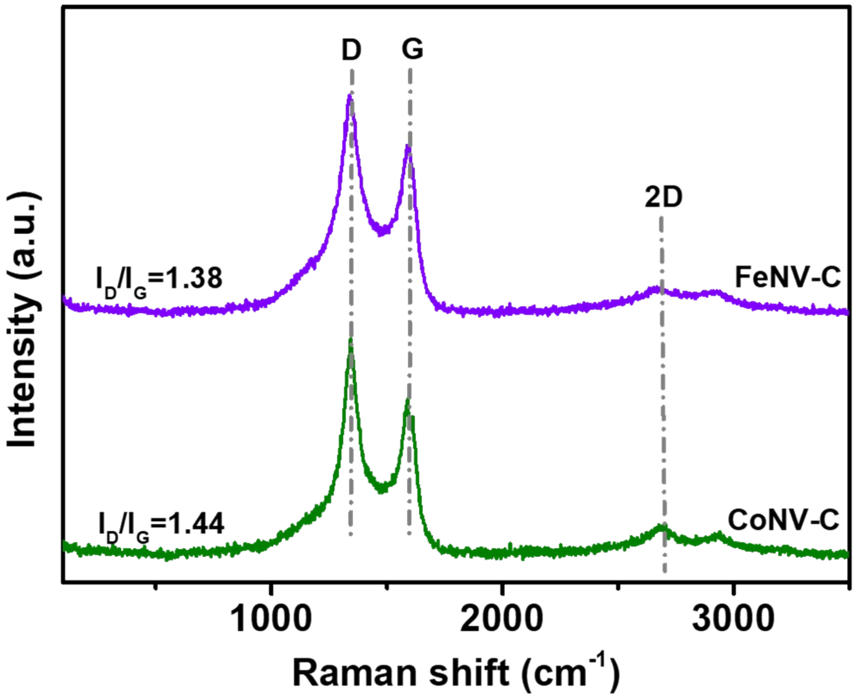

Fig. S18. Raman spectra for CoNV-C and FeNV-C. the I_D/I_G values for CoNV-C and FeNV-C were reached to 1.44 and 1.38, respectively, which indicated that amounts of defects were produced in CoNV-C and FeNV-C.

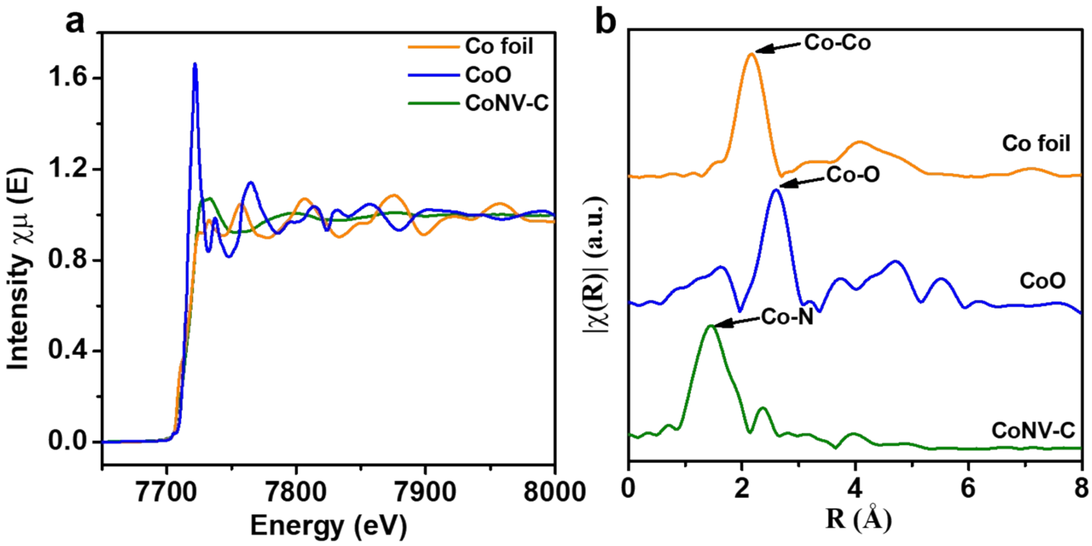

Fig. S19. a) Co K-edge XANES spectra for Co foil, CoO and CoNV-C. **b)** Fourier transformation of the EXAFS spectra of Co foil, CoO and CoNV-C. The main peak presence at approximately 1.45 Å for CoNV-C can be attributed to the Co-N first shell. No Co-Co (2.18 Å) characteristic peak appear in the CoNV-C, revealing the atomically dispersed Co atoms.

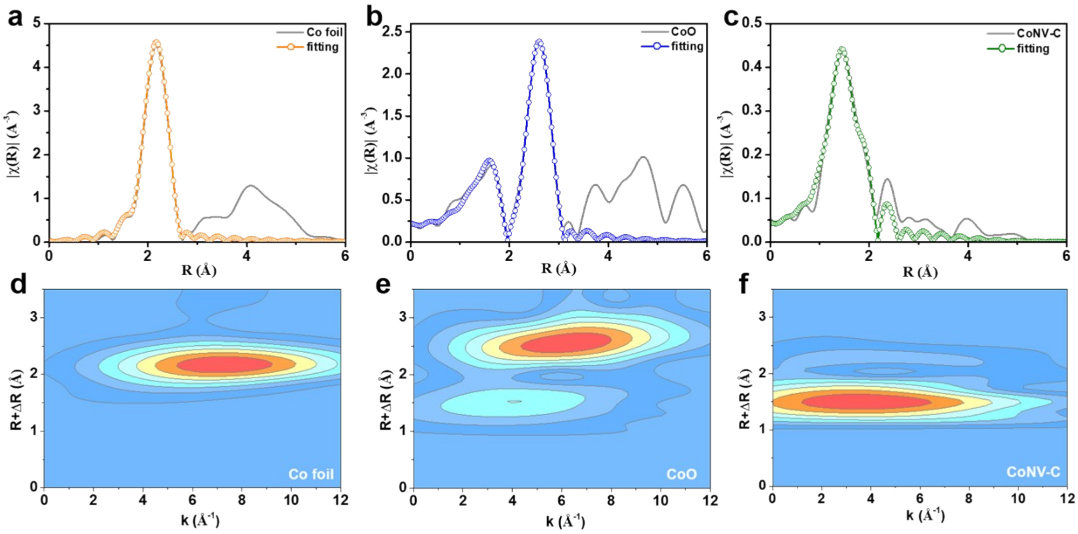

Fig. S20. a) Fourier transformation of EXAFS spectra fitting results of Co foil. **b)** Fourier transformation of EXAFS spectra fitting results of CoO. **c)** Fourier transformation of EXAFS spectra fitting results of CoNV-C, the Co-N coordination numbers in CoNV-C was 1.7. **d)**, **e)**, and **f)** EXAFS wavelet transform plots for Co foil, CoO and CoNV-C.

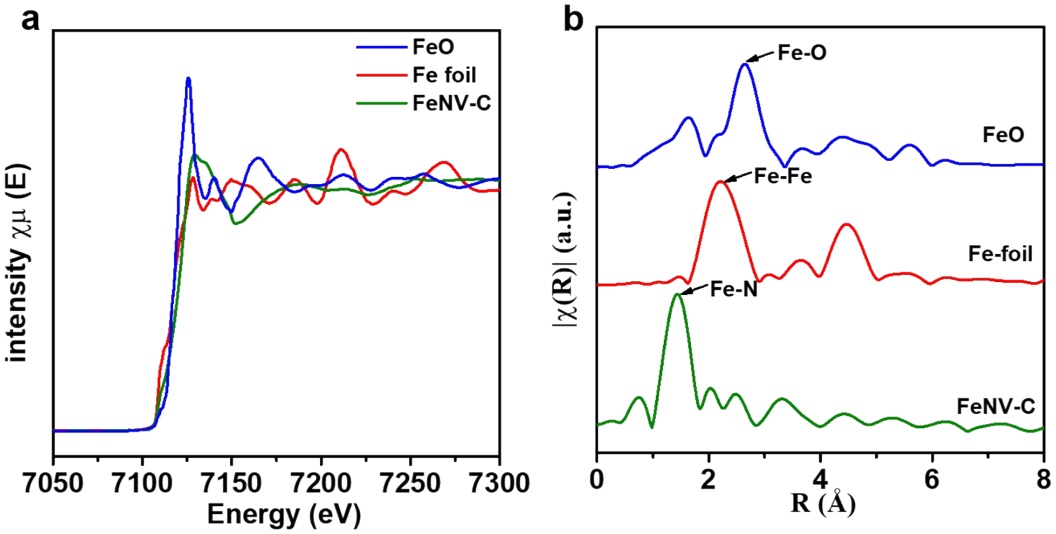

Fig. S21. a) Fe K-edge XANES spectra of Fe foil, FeO, and FeNV-C. **b)** Fourier transformation of the EXAFS spectra of Fe foil, FeO, and FeNV-C. The main peak presented at approximately 1.48 Å for FeNV-C can be attributed to the Fe-N first shell. No Fe-Fe (2.34 Å) characteristic peak appeared in FeNV-C, revealing the atomically dispersed Fe species.

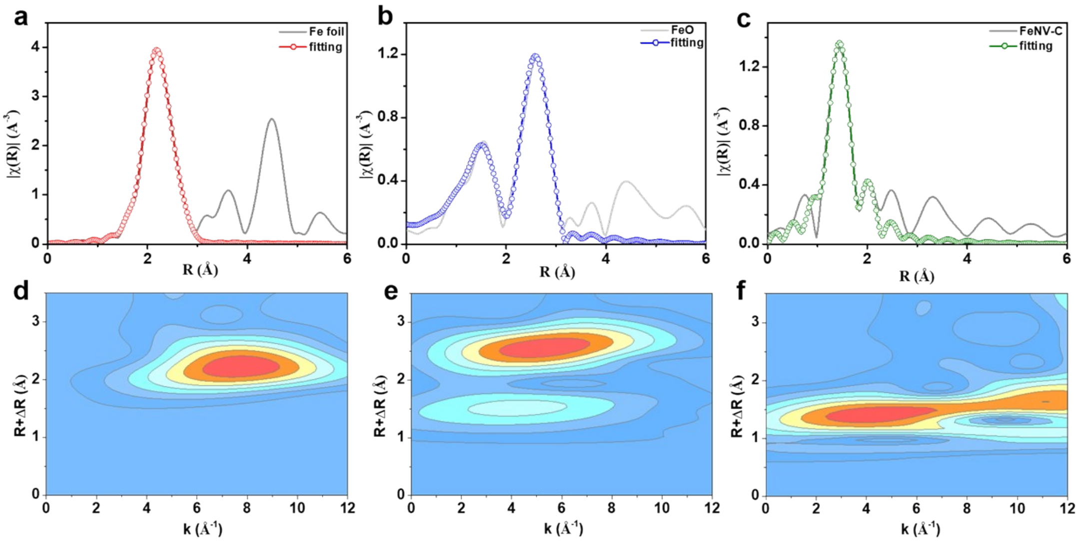

Fig. S22. a) Fourier transformation of EXAFS spectra fitting results of Fe foil. **b)** Fourier transformation of EXAFS spectra fitting results of FeO. **c)** Fourier transformation of EXAFS spectra fitting results of FeNV-C, the Fe-N coordination numbers in FeNV-C was 2.9. **d)**, **e)**, and **f)** EXAFS wavelet transform plots for Fe foil, FeO and FeNV-C.

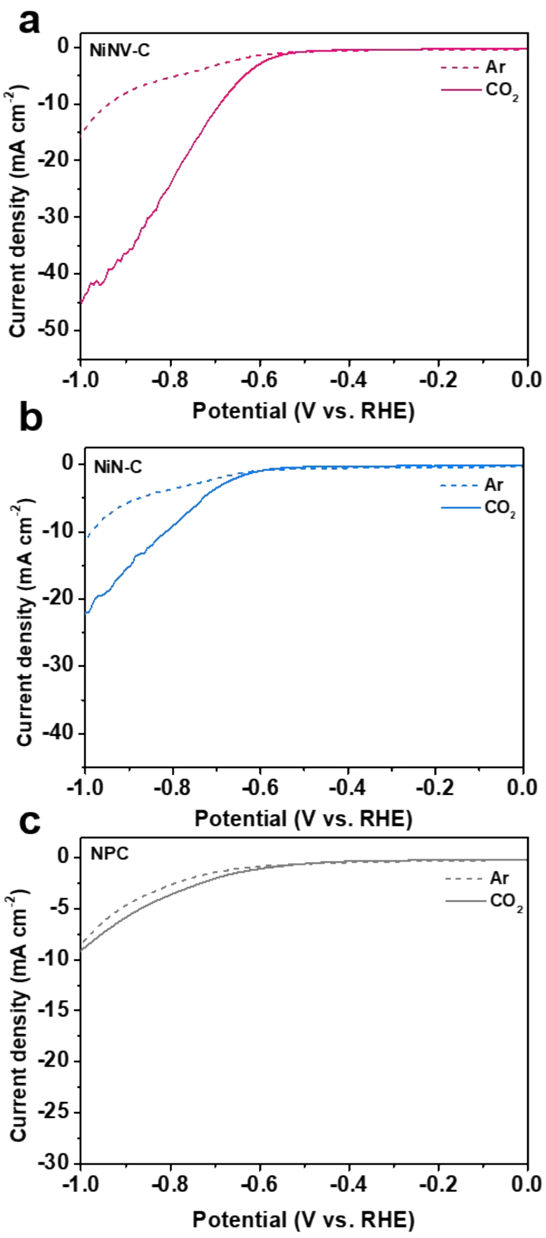

Fig. S23. The liner sweep voltammetry (LSV) curves test in Ar and CO_2-saturated 0.5 M $KHCO_3$. a) NiNV-C; **b)** NiN-C; **c)** NPC. Compared with the polarization curves in Ar-saturated electrolyte, NiNV-C and NiN-C exhibited a larger current density in CO_2-saturated electrolyte, suggesting the high activity toward CO_2 reduction.

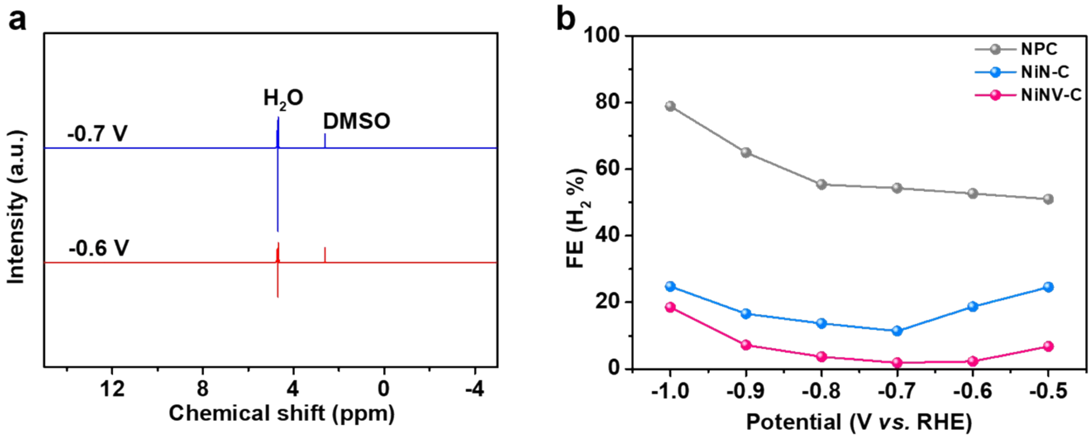

Fig. S24. CO_2RR performance for NiN-C, NiNV-C, and NPC. a) ^1H nuclear magnetic resonance (NMR) spectroscopy for NiNV-C products after reaction. Only water and solvent signal was detected, which indicated that no liquid products formation during CO_2RR. **b)** H_2 Faradaic efficiency for NiN-C, NiNV-C and NPC at various specific potentials.

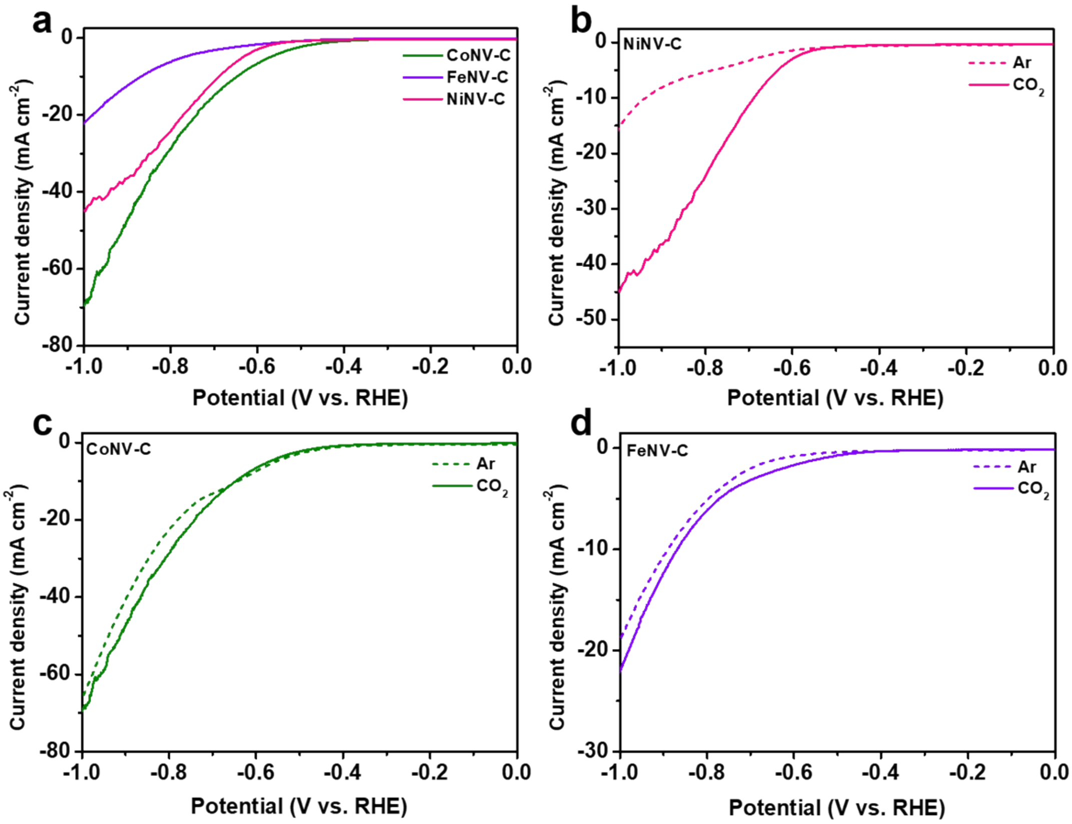

Fig. S25. LSV curves of as-prepared SACs in Ar and CO_2-saturated electrolyte. a) LSV curves of CoNV-C, FeNV-C and NiNV-C in CO_2-saturated electrolyte. **b)**, **c)**, and **d)** Comparing LSV curves of NiNV-C, CoNV-C, and FeNV-C in Ar and CO_2-saturated electrolyte.

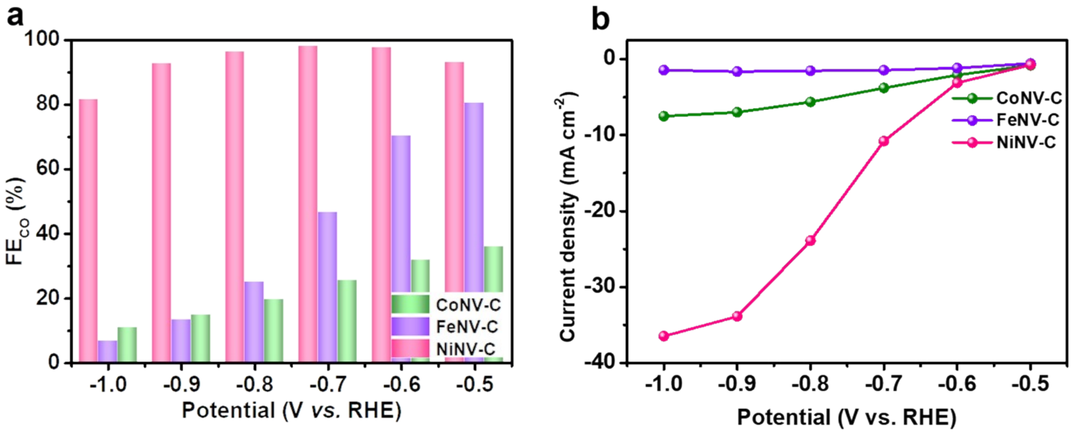

Fig. S26. CO_2RR performance for NiNV-C, FeNV-C, and CoNV-C. **a)** CO FE for NiNV-C, FeNV-C, and CoNV-C at various specific potentials. NiNV-C exhibited the highest FE for CO formation, the maximum CO FE for CoNV-C and FeNV-C was 61 % and 78 %, respectively. The low conversion efficiency could be attributed to the compete hydrogen evolution reaction on Co and Fe sites. **b)** CO partial current density values for NiNV-C, FeNV-C, and CoNV-C.

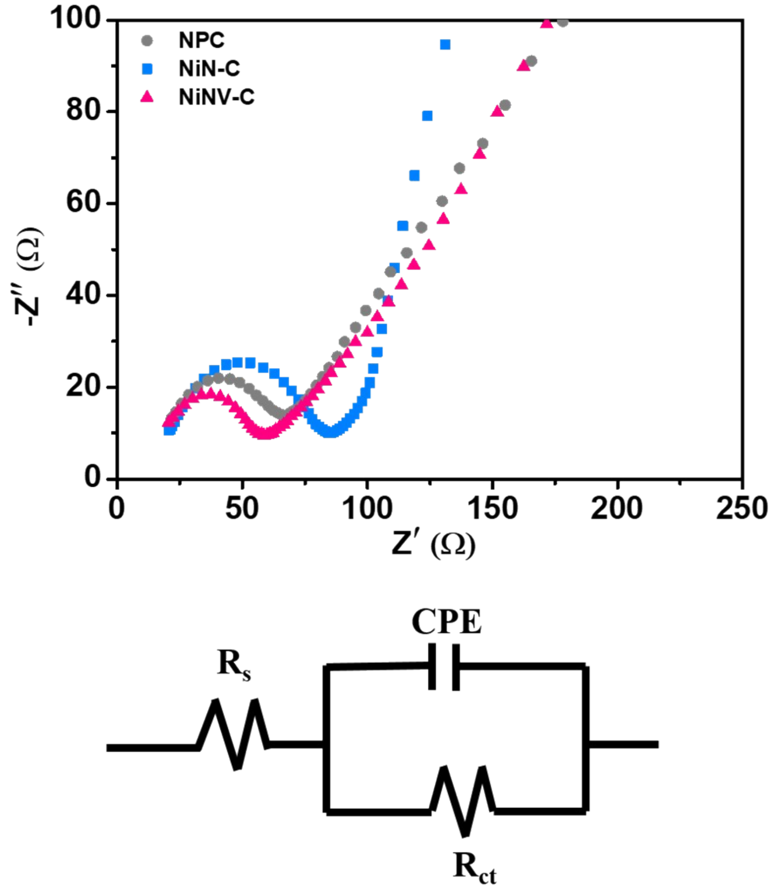

Fig. S27. The Nyquist plots and corresponding equivalent circuit of EIS. NiNV-C and NPC show the better conductivity than that of NiN-C, which can be attributed to the second heat treatment under high temperature.

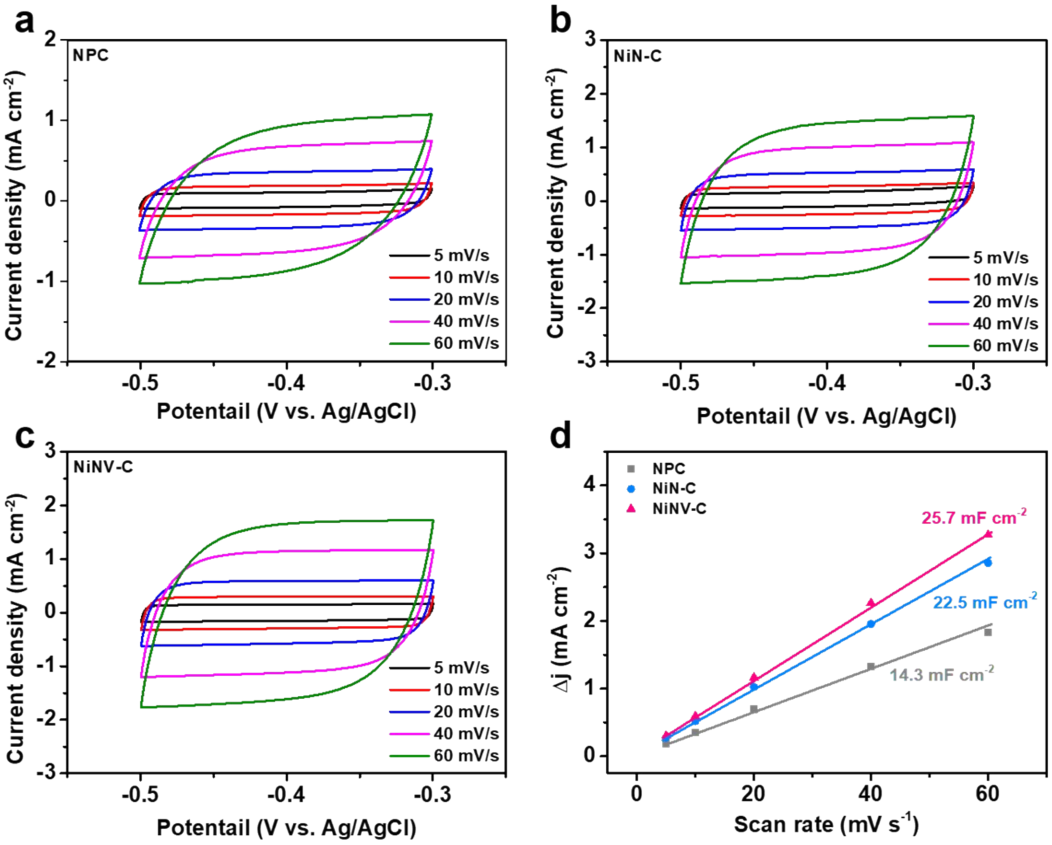

Fig. S28. CV curves measured at scan rates varying from 5 to 60 mV s^{-1}. a) CV curves of NPC; **b)** CV curves of NiN-C; **c)** CV curves of NiNV-C; **d)** C_{dl} of NPC, NiN-C, and NiNV-C calculated from CV curves. NiNV-C showed the higher C_{dl} than that of NPC and NiN-C.

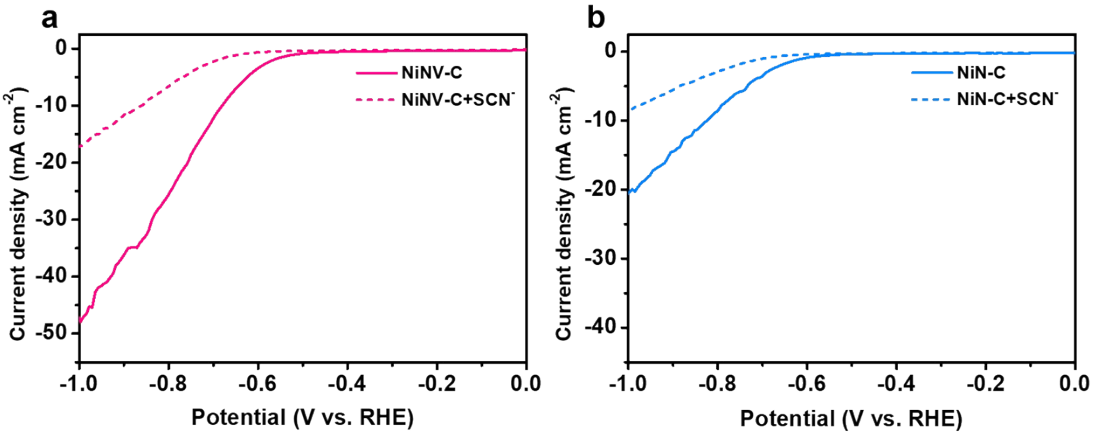

Fig. S29. SCN$^-$ poisoning experiments. a) Polarization curves of NiNV-C with or without SCN$^-$. **b)** Polarization curves of NiN-C with or without SCN$^-$. Obvious attenuation of current density was happened after introduce SCN$^-$ into the electrolyte, which can be attributed to the blockage of Ni species by the strong interaction between Ni and SCN$^-$.

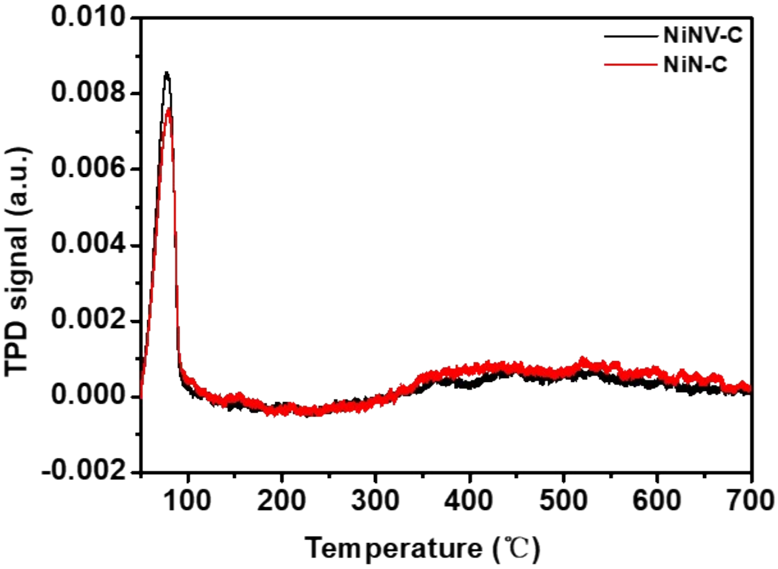

Figure S30. CO TPD profiles of NiNV-C and NiN-C. The CO desorption quantify of NiNV-C and NiN-C is 43.2 and 42.2 µmol g^{-1}, respectively.

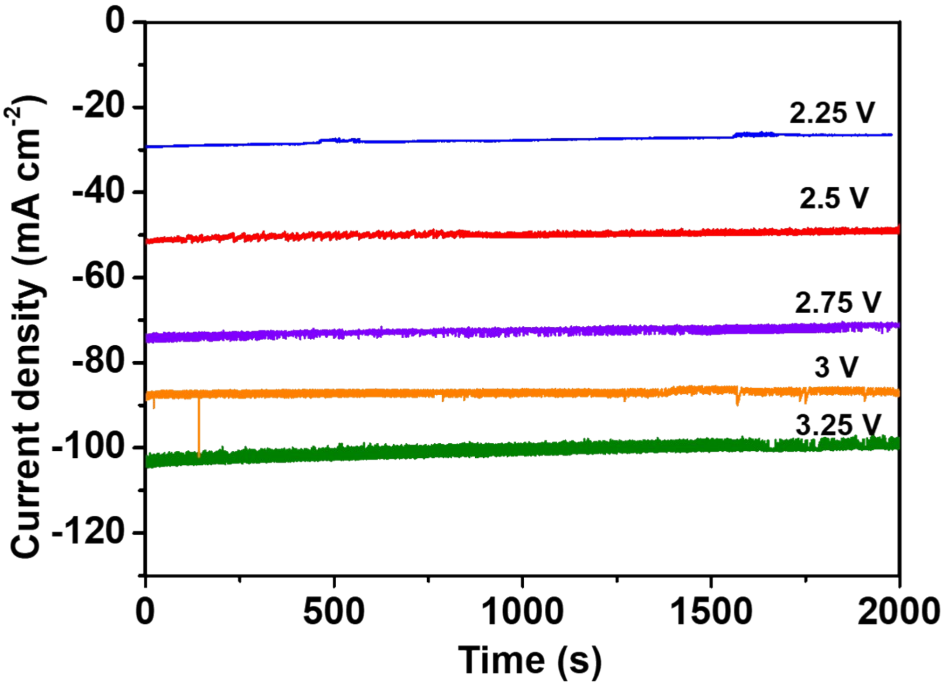

Fig. S31. Current density measured at different potential in flow cell. Higher current density was obtained in flow cell reactor.

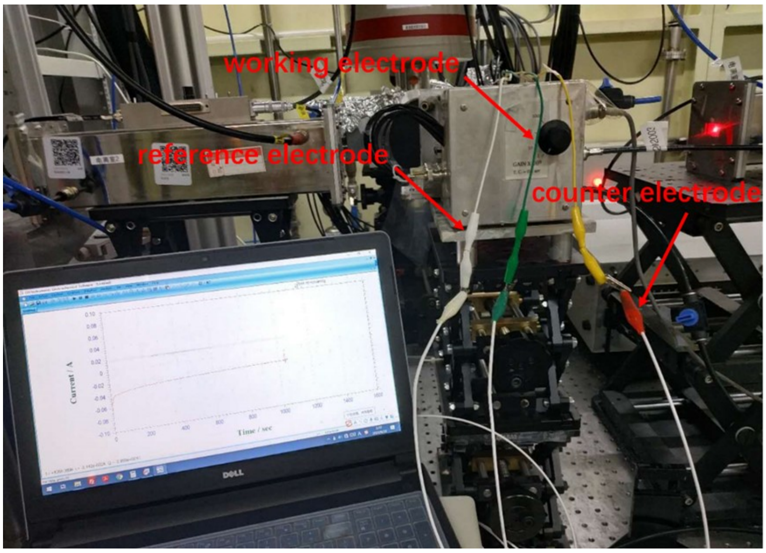

Fig. S32. Photo of operando X-ray adsorption spectroscopy measurements.

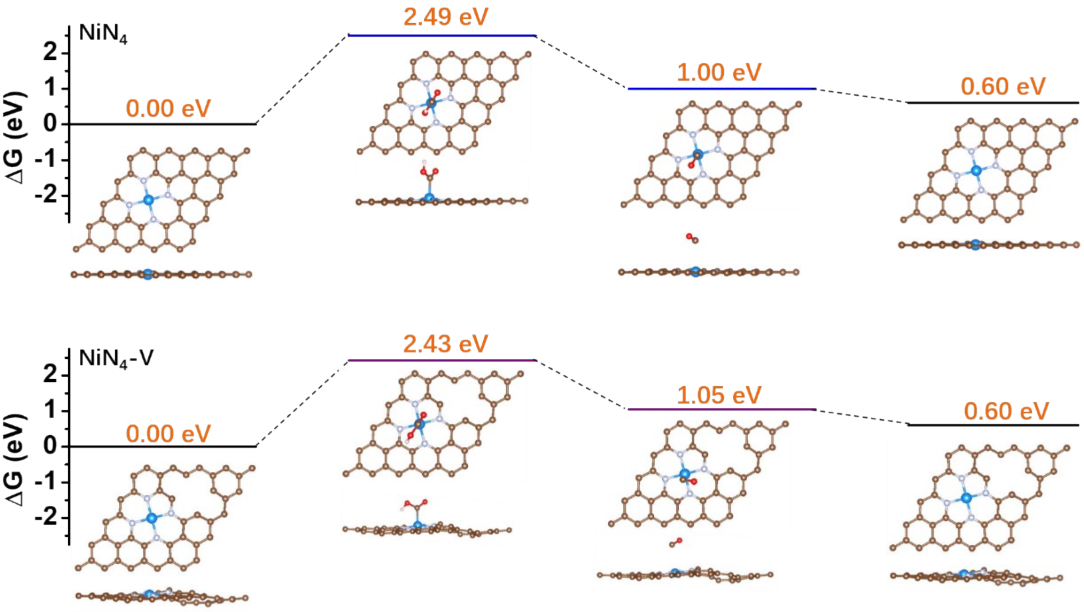

Fig. S33. Theoretical simulation CO_2 reduction on NiN$_4$ (top) and NiN$_4$-V (down) models. The free energy for *COOH formation (limit step in CO_2RR) was 2.49 and 2.43 eV, respectively.

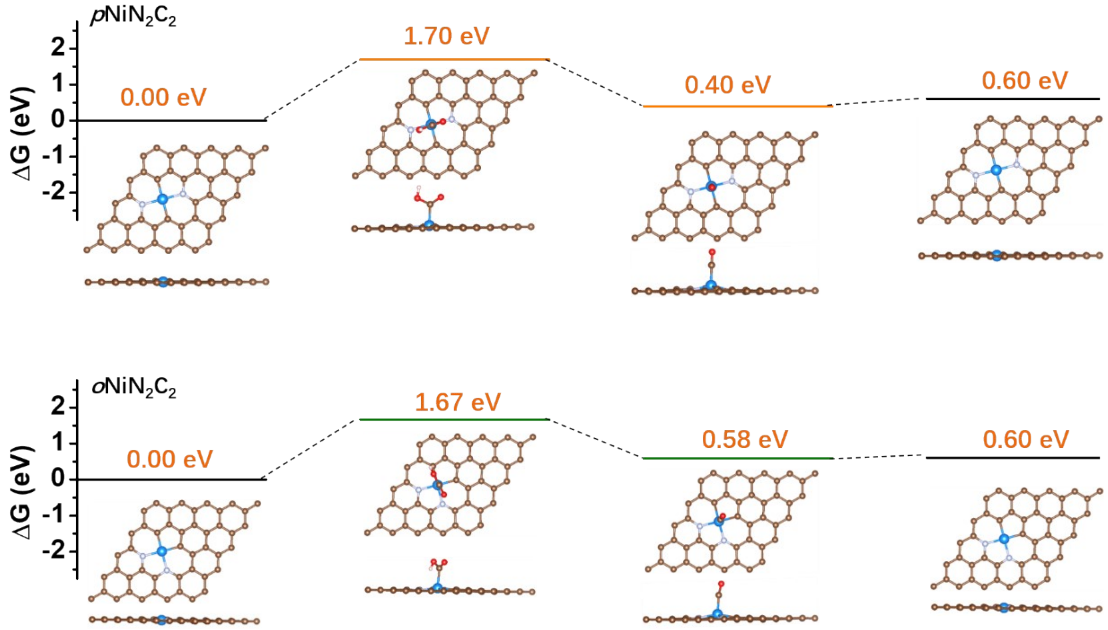

Fig. S34. Theoretical simulation CO_2 reduction on *p*NiN_2C_2 (top) and *o*NiN_2C_2 (down) models. The free energy for *COOH formation (limit step in CO_2RR) was 1.70 and 1.67 eV, respectively.

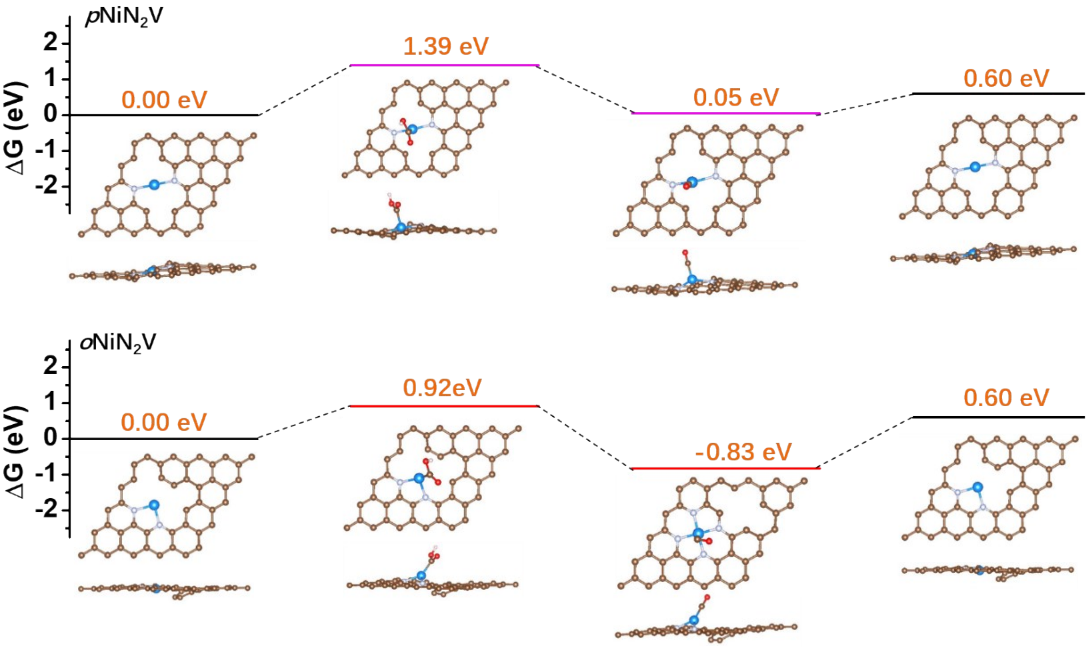

Fig. S35. Theoretical simulation CO_2 reduction on *p*NiN_2V (top) and *o*NiN_2V (down) models. The free energy for *COOH formation was 1.39 and 0.92 eV, respectively, which was lower than that of above NiN_4 and NiN_2C_2 models.

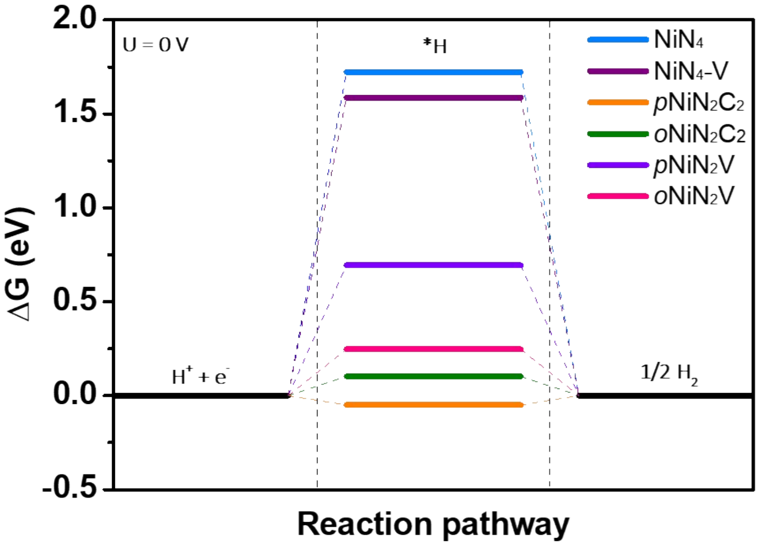

Figure S36. Schematic Gibbs free energy profile for the HER on different active site.

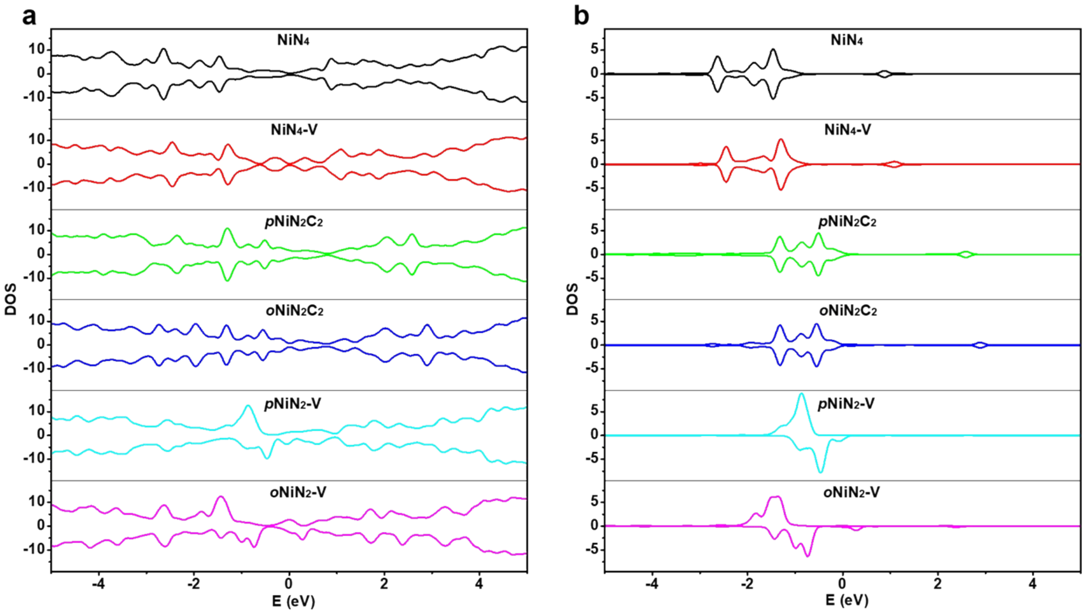

Fig. S37. a) The calculated PDOS of optimized models. **b)** The calculated PDOS of the Ni 3d orbital in optimized models. The PDOS of *p*NiN$_2$V and *o*NiN$_2$V showed asymmetry of spin-up and spin-down, primarily attributed to the spin polarization of Ni species.

3. Supplementary Tables

Table S1. Optimal fitting EXAFS data for NiN-C and NiNV-C.

Sample	shell	N	R (Å)	σ^2 (10^{-3}Å^2)	ΔE_0	R factor
Ni foil	Ni-Ni	12	2.49±0.01	7.5±0.3	6.9±0.8	0.01
NiO	Ni-O	6	2.09±0.01	5.6±1.6	3.0±1.9	0.014
	Ni-Ni	12	2.95±0.02	6.2±0.6		
NiN-C	Ni-N	3.8	1.84±0.02	9.2±1.8	0.1±3.6	0.01
	Ni-C	4.1	2.54±0.02	8.6±2.9		
NiNV-C	Ni-N	2.3	1.84±0.02	4.9±0.9	2.4±1.9	0.016
	Ni-C	1.8	2.51±0.05	9.3±0.7		

N: coordination number, the Ni-Ni coordination numbers in Ni foil was fixed as 12; R: distance between absorber and backscatter atoms; σ^2: Debye–Waller factor to account for both thermal and structural disorders; ΔE_0: inner potential correction; R factor: goodness of the fit. S_0^2 was fixed to 0.95 as determined from Ni foil fitting.

Table S2. Optimal fitting EXAFS data for Fe foil, FeO and FeNV-C.

Sample	shell	N	R (Å)	σ^2 (10^{-3}Å^2)	ΔE_0	R factor
Fe foil	Fe-Fe (1st)	8	2.47±0.01	6.5±0.4	4.9±1.6	0.01
	Fe-Fe (2nd)	6	2.84±0.01	7.0±1.0		
FeO	Fe-O	6	2.10±0.02	19.2±2.4	-3.1±1.3	0.023
	Fe-Fe	12	3.06±0.01	16.3±0.9		
FeNV-C	Fe-N	2.9	1.91±0.03	0.7±4.1	-0.9±3.1	0.008
	Fe-C	2.1	2.56±0.07	2.0±9.6		

N: coordination number, the Fe coordination numbers in Fe foil was fixed as 8 and 6 in first and second shell; R: distance between absorber and backscatter atoms; σ^2: Debye–Waller factor to account for both thermal and structural disorders; ΔE_0: inner potential correction; R factor: goodness of the fit. S_0^2 was fixed to 0.91 as determined from Fe foil fitting.

Table S3. Optimal fitting EXAFS data for Co foil, CoO and CoNV-C.

Sample	shell	N	R (Å)	σ^2 (10^{-3}Å^2)	ΔE_0	R factor
Co foil	Co-Co	12	2.49±0.003	7.2±0.2	7.1±0.6	0.005
CoO	Co-O	6	2.10±0.01	9.9±1.6	-2.0±1.0	0.014
	Co-Co	12	3.00±0.01	9.2±0.5		
CoNV-C	Co-N	1.7	1.90±0.03	12.3±4.3	8.5±3.3	0.016
	Co-C	1.8	2.47±0.03	3.1±2.3		

N: coordination number, the Co-Co coordination numbers in Co foil was fixed as 12; R: distance between absorber and backscatter atoms; σ^2: Debye–Waller factor to account for both thermal and structural disorders; ΔE_0: inner potential correction; R factor: goodness of the fit. S_0^2 was fixed to 0.85 as determined from Co foil fitting.

Table S4. Elemental analysis of NPC, NiNV-C and NiN-C based on XPS analysis and ICP (wt.%)

Sample	**C**	**N**	**Mg**	**Ni**	
NiNV-C	97.68	1.24	0.63	0.45	(0.52 by ICP)
NiN-C	96.45	2.14	0.66	0.55	(0.63 by ICP)
NPC	98.12	1.18	0.70	/	

Table S5. N_2 adsorption/desorption measurements for NiN-C, NiNV-C and NPC.

Sample	S_{BET} ($m^2\ g^{-1}$)[a]	S_{micro} ($m^2\ g^{-1}$)[b]	V_{Tot} ($cm^3\ g^{-1}$)[c]	V_{micro} ($cm^3\ g^{-1}$)[d]	D_{av} (nm)[e]
NiN-C	566	51	1.812	0.024	12.8
NiNV-C	586	59	1.941	0.031	13.2
NPC	617	14	1.654	0.004	10.7

[a] Specific surface area measured by BET model; [b] The microporous surface area analyzed by t-plot method; [c] The total pore volume measured at $P/P_0 = 0.99$; [d] The microporous volume analyzed by t-plot method; e) Average pore size.

Table S6. R_{ct} values of NiN-C, NiNV-C and NPC.

Sample	Rct
NiN-C	53
NiNV-C	40
NPC	47

Table S7. Comparison of CO_2RR performance with reported electrocatalysts.

Catalysts	Electrolyte	Onset potential (mV, vs RHE)	Over potential (mV, vs RHE)	Current density (mA/cm^2)	Faradaic efficiency	Reference
Au nanoneedle	0.5 M $KHCO_3$	200	240	15	94%	[1]
Nanoporous Ag	0.5 M $KHCO_3$	/	390	8	92%	[2]
COF-367-Co	0.5 M $KHCO_3$	420	560	0.4	91%	[3]
MOF-Co	0.5 M $KHCO_3$	450	590	1	76%	[4]
Co porphyrin	1 mM $HClO_4$+99 mM $NaClO_4$	/	500	0.16	60%	[5]
Fe porphyrin organic cage	0.5 M $KHCO_3$	/	520	0.5	100%	[6]
Ni coordinate CTF	0.5 M $KHCO_3$	480	690	2	90%	[7]
Ni Sas/N-C	0.5 M $KHCO_3$	570	890	10.5	70.3%	[8]
Ni-N-C	0.5 M $KHCO_3$	/	560	3.2	93%	[9]
Ni-N-C	0.1 M $KHCO_3$	580	670	9	85%	[10]
Ni-GS	0.5 M $KHCO_3$	290	640	21.3	96%	[11]
NiPor-CTF	0.5 M $KHCO_3$	443	490	7.0	91 %	[12]
A-Ni-NG	0.5 M $KHCO_3$	180	610	31.5	97%	[13]
Ni-N_4-C	0.5 M $KHCO_3$	/	700	28.6	99%	[14]
Ni-N-GO	0.1 M $KHCO_3$	500	590	2.5	95%	[15]
Ni-N-Graphene	0.1 M $KHCO_3$	/	620	11	95%	[16]
Ni@NCH-1000	0.1 M $KHCO_3$	/	890	35	96%	[17]
Ni-N-C	0.1 M $KHCO_3$	/	640	8.2	96%	[18]
Ni-NCB	0.1 M $KHCO_3$	410	680	10.5	99%	[19]

NiSA@N-C	0.1 M $KHCO_3$	/	750	26.4	96%	[20]
Cu-N2/NG	0.1 M $KHCO_3$	330	500	2.1	81%	[21]
C-Zn1Ni4 ZIF-8	0.5 M $KHCO_3$	/	520	4.7	94.5%	[22]
NiSA-NGA	0.5 M $KHCO_3$	/	690	6.4	90.2%	[23]
Ni-N2-C2	0.5 M $KHCO_3$	/	690	15	98%	[24]
Ni-N3-V	0.5 M $KHCO_3$	/	590	48	94%	[25]
NiNV-C	**0.5 M $KHCO_3$**	**456**	**590**	**10.3**	**98.4%**	**This work**
	1 M KOH Flow cell	**/**	**2.5 V (E_{cell})**	**51**	**99.7%**	**This work**

Reference:

[1]. Liu, M.; Pang, Y.; Zhang, B.; De Luna, P.; Voznyy, O.; Xu, J.; Zheng, X.; Dinh, C. T.; Fan, F.; Cao, C.; de Arquer, F. P. G.; Safaei, T. S.; Mepham, A.; Klinkova, A.; Kumacheva, E.; Filleter, T.; Sinton, D.; Kelley, S. O.; Sargent, E. H., *Nature,* 2016, **537**, 382.

[2]. Lu, Q.; Rosen, J.; Zhou, Y.; Hutchings, G. S.; Kimmel, Y. C.; Chen, J. G.; Jiao, F., *Nat. Commun.*, 2014, **5**, 3242.

[3]. Lin, S.; Diercks, C. S.; Zhang, Y.-B.; Kornienko, N.; Nichols, E. M.; Zhao, Y.; Paris, A. R.; Kim, D.; Yang, P.; Yaghi, O. M.; Chang, C. J., *Science,* 2015, **349**, 1208.

[4]. Kornienko, N.; Zhao, Y.; Kley, C. S.; Zhu, C.; Kim, D.; Lin, S.; Chang, C. J.; Yaghi, O. M.; Yang, P., *J. Am. Chem. Soc.,* 2015, **137**, 14129.

[5]. Shen, J.; Kortlever, R.; Kas, R.; Birdja, Y. Y.; Diaz-Morales, O.; Kwon, Y.; Ledezma-Yanez, I.; Schouten, K. J. P.; Mul, G.; Koper, M. T. M., *Nat. Commun.*, 2015, **6**, 8177.

[6]. Smith, P. T.; Benke, B. P.; Cao, Z.; Kim, Y.; Nichols, E. M.; Kim, K.; Chang, C. J., *Angew. Chem., Int. Ed.*, 2018, **57**, 9684.

[7]. Su, P.; Iwase, K.; Harada, T.; Kamiya, K.; Nakanishi, S., *Chem. Sci.*, 2018, **9**, 3941.

[8]. Zhao, C.; Dai, X.; Yao, T.; Chen, W.; Wang, X.; Wang, J.; Yang, J.; Wei, S.; Wu, Y.; Li, Y., *J. Am. Chem. Soc.*, 2017, **139**, 8078.

[9]. Hu, X.-M.; Hval, H. H.; Bjerglund, E. T.; Dalgaard, K. J.; Madsen, M. R.; Pohl, M.-M.; Welter, E.; Lamagni, P.; Buhl, K. B.; Bremholm, M.; Beller, M.; Pedersen, S. U.; Skrydstrup, T.; Daasbjerg, K., *ACS Catal.*, 2017, **8**, 6255.

[10]. Ju, W.; Bagger, A.; Hao, G.-P.; Varela, A. S.; Sinev, I.; Bon, V.; Roldan Cuenya, B.; Kaskel, S.; Rossmeisl, J.; Strasser, P., *Nat. Commun.*, 2017, **8**, 944.

[11]. Jiang, K.; Siahrostami, S.; Akey, A. J.; Li, Y.; Lu, Z.; Lattimer, J.; Hu, Y.; Stokes, C.; Gangishetty, M.; Chen, G.; Zhou, Y.; Hill, W.; Cai, W.-B.; Bell, D.; Chan, K.; Nørskov, J. K.; Cui, Y.; Wang, H., *Chem*, 2017, **3**, 950.

[12]. Lu, C.; Yang, J.; Wei, S.; Bi, S.; Xia, Y.; Chen, M.; Hou, Y.; Qiu, M.; Yuan, C.; Su, Y.; Zhang, F.; Liang, H.; Zhuang, X., *Adv. Funct. Mater.*, 2019, **29**, 1806884.

[13]. Yang, H. B.; Hung, S.-F.; Liu, S.; Yuan, K.; Miao, S.; Zhang, L.; Huang, X.; Wang, H.-Y.; Cai, W.; Chen, R.; Gao, J.; Yang, X.; Chen, W.; Huang, Y.; Chen, H. M.; Li, C. M.; Zhang, T.; Liu, B., *Nat. Energy*, 2018, **3**, 140.

[14]. Li, X.; Bi, W.; Chen, M.; Sun, Y.; Ju, H.; Yan, W.; Zhu, J.; Wu, X.; Chu, W.; Wu, C.; Xie, Y., *J. Am. Chem. Soc.*, 2017, **139**, 14889.

[15]. Su, P.; Iwase, K.; Nakanishi, S.; Hashimoto, K.; Kamiya, K., *Small*, 2016, **12**, 6083.

[16]. Jiang, K.; Siahrostami, S.; Zheng, T.; Hu, Y.; Hwang, S.; Stavitski, E.; Peng, Y.; Dynes, J.; Gangisetty, M.; Su, D.; Attenkofer, K.; Wang, H., *Energy Environ. Sci.*, 2018, **11**, 893.

[17]. Daiyan, R.; Zhu, X.; Tong, Z.; Gong, L.; Razmjou, A.; Liu, R.-S.; Xia, Z.; Lu, X.; Dai, L.; Amal, R., *Nano Energy*, 2020, **78**, 105213.

[18]. Pan, F.; Deng, W.; Justiniano, C.; Li, Y., *Appl. Catal. B*, 2018, **226**, 463.

[19]. Zheng, T.; Jiang, K.; Ta, N.; Hu, Y.; Zeng, J.; Liu, J.; Wang, H., *Joule*, 2019, **3**, 265.

[20]. Lu, Y.; Wang, H.; Yu, P.; Yuan, Y.; Shahbazian-Yassar, R.; Sheng, Y.; Wu, S.; Tu, W.; Liu, G.; Kraft, M.; Xu, R., *Nano Energy*, 2020, **77**, 105158.

[21]. Zheng, W.; Yang, J.; Chen, H.; Hou, Y.; Wang, Q.; Gu, M.; He, F.; Xia, Y.; Xia, Z.; Li, Z.; Yang, B.; Lei, L.; Yuan, C.; He, Q.; Qiu, M.; Feng, X., *Adv. Funct. Mater.*, 2020, **30**, 1907658

[22]. Yan, C.; Li, H.; Ye, Y.; Wu, H.; Cai, F.; Si, R.; Xiao, J.; Miao, S.; Xie, S.; Yang, F.; Li, Y.; Wang, G.; Bao, X., *Energy Environ. Sci.*, 2018, **11**, 1204.

[23]. Mou, K.; Chen, Z.; Zhang, X.; Jiao, M.; Zhang, X.; Ge, X.; Zhang, W.; Liu, L., *Small*, 2019, **15**, 1903668.

[24]. Gong, Y.-N.; Jiao, L.; Qian, Y.; Pan, C.-Y.; Zheng, L.; Cai, X.; Liu, B.; Yu, S.-H.; Jiang, H.-L., *Angew. Chem., Int. Ed.*, 2020, **59**, 2705.

[25]. Rong, X.; Wang, H.-J.; Lu, X.-L.; Si, R.; Lu, T.-B., *Angew. Chem., Int. Ed.*, 2020, **59**, 1961.